



# The effect of octahedral distortions on the electronic properties and magnetic interactions in O3 NaTMO2 compounds (TM = Ti Ni & Zr Pd)

著者	Assadi M. Hussein N., Shigeta Yasuteru
journal or publication title	RSC Advances
volume	8
number	25
page range	13842-13849
year	2018-09
権利	(C) The Royal Society of Chemistry 2018 Open Access Article. Published on 13 April 2018. Downloaded on 12/06/2018 03:36:37. This article is licensed under a Creative Commons Attribution 3.0 Unported Licence.
URL	<a href="http://hdl.handle.net/2241/00152002">http://hdl.handle.net/2241/00152002</a>

doi: 10.1039/C8RA00576A

Cite this: *RSC Adv.*, 2018, 8, 13842

# The effect of octahedral distortions on the electronic properties and magnetic interactions in O3 NaTMO<sub>2</sub> compounds (TM = Ti–Ni & Zr–Pd)

M. Hussein N. Assadi \* and Yasuteru Shigeta

The interplay between the coordination environment and magnetic properties in O3 layered sodium transition metal oxides (NaTMO<sub>2</sub>) is a fascinating and complex problem. Through detailed and comprehensive density functional investigations on O3 NaTMO<sub>2</sub> compounds, we demonstrate that the TM ions in O3 NaMnO<sub>2</sub>, NaFeO<sub>2</sub> and NaCoO<sub>2</sub> adopt a high spin state. Structurally, NaMnO<sub>2</sub> and NaPdO<sub>2</sub> undergo Jahn–Teller distortions while NaNbO<sub>2</sub> undergoes puckering distortion. Furthermore, in addition to Jahn–Teller distortion, NaPdO<sub>2</sub> exhibits charge disproportionation as it contains Pd<sup>2+</sup>, Pd<sup>3+</sup> and Pd<sup>4+</sup> species. These distortions stabilize the inter-plane ferromagnetism. Additionally, the inter-plane ferromagnetic coupling is stabilized by kinetic p–d exchange mechanism in undistorted NaCoO<sub>2</sub>, NaNiO<sub>2</sub> and NaTcO<sub>2</sub>. The intra-plane coupling in this family of compounds on the other hand was found to be generally weak. Only NaMnO<sub>2</sub>, NaNiO<sub>2</sub> and NaTcO<sub>2</sub> are predicted to show bulk ferromagnetism with estimated Curie temperatures below ~50 K.

Received 19th January 2018

Accepted 5th April 2018

DOI: 10.1039/c8ra00576a

rsc.li/rsc-advances

## 1. Introduction

Layered hexagonal compounds with formula NaTMO<sub>2</sub> in which TM is a transition metal often exhibit interesting magnetic,<sup>1–3</sup> thermoelectric,<sup>4</sup> and electrochemical properties.<sup>5</sup> One obstacle in studying these compounds is the rich variety of their polymorphs each with distinct symmetry and local coordination for the transition metal ions which complicates finding general property trends for this family of materials. One such area of research that lacks a concise overview is the magnetic properties of the NaTMO<sub>2</sub> compounds. For instance, reports of conflicting experimental observations of the magnetic properties for the same compound is not unheard of.<sup>6,7</sup> Such contradictions oftentimes stem from coarse structural characterization, restricted by instruments' range and resolution, which falls short in capturing the delicate structural details that dictate the magnetic ground state in these compounds.<sup>8,9</sup> This study therefore presents a detailed and focused density functional insight into one important family of such layered materials, namely O3 NaTMO<sub>2</sub> compounds in which TM is a fourth or fifth row transition metal element.

We start our investigations with compounds of  $R\bar{3}m$  symmetry which is a common symmetry group among layered compounds.<sup>10</sup> As shown in Fig. 1(a) and (b), the hexagonal representation of this structure consists of three alternating TMO<sub>2</sub> and Na layers. The notion "O3" indicates that oxygen ions are stacked in ABCABC order and Na ions occupy the octahedral

site with respect to the surrounding O ions. The primitive cell of the  $R\bar{3}m$  O3 structure, presented in Fig. 1(c), has rhombohedral symmetry and the TM ion is located in the center of the primitive cell coordinated by six oxygen ions. The O–TM–O angles, marked  $\eta$  in Fig. 1(c), depend on the lattice parameters of the rhombohedral primitive cell ( $a$  and  $\alpha$ ) and the fractional coordinates of oxygen. If this angle is not exactly 90°, then it follows that the O–TM–O angles alternate between values smaller and larger than 90° resulting in a rhombohedral distortion to the TMO<sub>6</sub> octahedra. These angles are marked  $\eta$  and  $\theta$  in Fig. 1(d). This distortion decreases the octahedral symmetry and splits the energy levels of the  $t_{2g}$  orbitals of the TM ions into a single  $a_{1g}$  orbital and doubly degenerate  $e'_{g}$  orbitals. The sequence of stabilization of the  $a_{1g}$  and  $e'_{g}$  orbitals is not however trivial.<sup>11</sup> In addition to the rhombohedral distortion which is inherent to the  $R\bar{3}m$  symmetry, NaTMO<sub>2</sub> compounds may also experience additional distortions that further reduce the overall symmetry and influence the electronic structure. We will thoroughly examine all such distortions and determine how they influence the electronic and magnetic properties of O3 NaTMO<sub>2</sub> compounds.

## 2. Computational and system settings

Spin polarized density functional theory (DFT) calculations were carried out within augmented plane-wave potential<sup>12</sup> formalism as implemented in VASP code.<sup>13,14</sup> Brillouin zone was sampled using a mesh generated by Monkhorst–Pack scheme with spacing of  $\sim 0.02 \text{ \AA}^{-1}$  among  $k$  points while the energy cut-off was set to 550 eV. The threshold for energy convergence was

Center for Computational Sciences, University of Tsukuba, Tennodai 1-1-1, Tsukuba, Ibaraki 305-8577, Japan. E-mail: h.assadi.2008@ieee.org



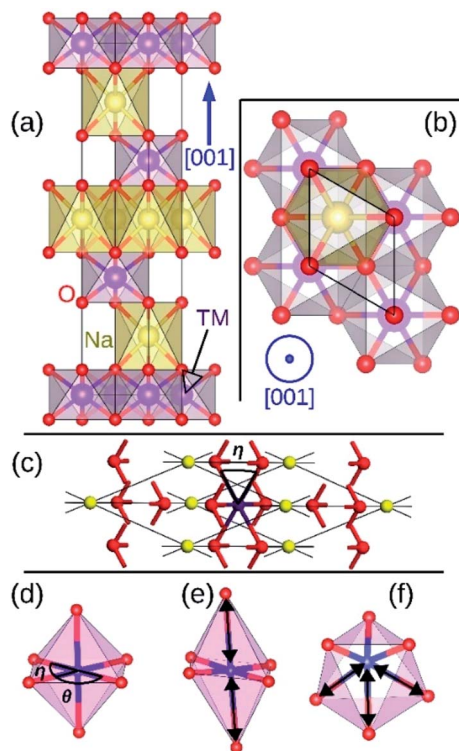


Fig. 1 The side view (a) and the top view (b) of O3 NaTMO<sub>2</sub> compounds in hexagonal representation. The same lattice structure in rhombohedral representation is shown in (c). O, TM and Na ions occupy 6c, 3b and 3a Wyckoff positions respectively. The rhombohedral, elongated Jahn–Teller and puckering distortions are presented in (d), (e) and (f) respectively. Elongated bonds are marked with double arrows.

set to 10<sup>−7</sup> eV per atom. Orbital population and bonding characteristics were examined using LOBSTER code.<sup>15</sup>

The exchange-correlation functional was approximated by the Perdew–Burke–Ernzerhof method.<sup>16,17</sup> To improve the electronic description of the compounds in term of localizing the d shell electrons of the transition metal elements, an orbital dependent Hubbard term<sup>18</sup> was applied to the d orbitals. The value of  $U_{\text{eff}}(U - J)$  was set to 5 eV for 3d TM elements and 2 eV for 4d TM elements. Weaker localization effects of the 4d electrons justifies the smaller  $U_{\text{eff}}$  value for the 4d elements. Among the different elements of the 3d and the 4d rows, a small variation in  $U_{\text{eff}}$  is naturally expected. However, the choice of constant  $U_{\text{eff}}$  for each row allows a more straightforward comparison.<sup>19</sup> This procedure is further justified by the fact that the localization effects in NaVO<sub>2</sub> are not affected by slight variation of  $U_{\text{eff}}$ .<sup>11</sup> Furthermore, as shown in Table 1, the applied  $U_{\text{eff}}$  values reproduce the lattice constants reported in earlier experiments within ~1% deviation indicating the adequacy of the chosen values.

O3 NaTMO<sub>2</sub> structure with  $R\bar{3}m$  symmetry in hexagonal representation, as shown in Fig. 1(a) and (b), was initially used for all compounds. To find the final geometries of NaTMO<sub>2</sub> compounds, the lattice parameters and all internal coordinates of the primitive cell were allowed to relax to forces smaller than

0.001 eV Å<sup>−1</sup>. Furthermore, the geometry optimization was repeated with  $2a \times 2a \times 1c$ ,  $3a \times 3a \times 1c$  and  $4a \times 4a \times 1c$  supercells with symmetry restrictions turned off, to detect any possible distortion that may lower the total energy by breaking the symmetry.

The magnetic phase stability was examined by comparing the total energies of the ferromagnetic system ( $E_{\text{FM}}^t$ ) with those of competing antiferromagnetic phases. The energy of the ferromagnetic state was calculated by aligning the spin of the all TM ions in the hexagonal cell parallel. The total energy of the C-type antiferromagnetic state ( $E_{\text{CAFM}}^t$ ) was calculated by aligning the spin of adjacent TM ions within the basal planes of a  $2a \times 1a \times 1c$  supercell antiparallel.  $\Delta E_{\text{CAFM}}$  is defined as the difference between total energies  $E_{\text{CAFM}}^t$  and  $E_{\text{FM}}^t$  the per TM ion:

$$\Delta E_{\text{CAFM}} = [(E_{\text{CAFM}}^t/2) - E_{\text{FM}}^t]/n \quad (1)$$

Here,  $n$  is the total number of the TM ions in the ferromagnetic supercell which is 3 for systems without distortions but larger for distorted systems. The energy of the A-type antiferromagnetic states ( $E_{\text{AAFM}}^t$ ) calculated by aligning the spin of TM ions in a  $1a \times 1a \times 2c$  supercell antiparallel in alternating manner.  $\Delta E_{\text{AAFM}}$  is defined as the difference between  $E_{\text{AAFM}}^t$  and  $E_{\text{FM}}^t$  the per TM ion:

$$\Delta E_{\text{AAFM}} = [(E_{\text{AAFM}}^t/2) - E_{\text{FM}}^t]/n \quad (2)$$

Positive  $\Delta E_{\text{CAFM}}$  values indicate the preference of TM ion to align ferromagnetically within a TMO<sub>2</sub> plane (inter-plane) while positive  $E_{\text{AAFM}}^t$  indicate the preference of ferromagnetic coupling across TMO<sub>2</sub> planes (intra-plane).

## 3. Results and discussions

### 3.1. TM spin state

Based on the calculated spin populations presented in Table 2, the early 3d TM ions in NaTiO<sub>2</sub>, NaVO<sub>2</sub> and NaCrO<sub>2</sub> generally conform to the octahedral crystal field splitting  $t_{2g}e_g$ . However, as we will see later, there are finer splittings among  $t_{2g}$  states caused by symmetry considerations. Later TM ions in NaMnO<sub>2</sub>, NaFeO<sub>2</sub> and NaCoO<sub>2</sub> compounds stabilize in high spin configuration. We found that the total energy of the NaMnO<sub>2</sub> compound rose by 1.306 eV/f.u. (f.u. is formula unit) when the Mn ion was set to low spin configuration ( $t_{2g}^4e_g^0$ ). Similarly, the total energy of low spin NaFeO<sub>2</sub> ( $t_{2g}^5e_g^0$ ) rose by 0.889 eV/f.u. and the total energy of low spin NaCoO<sub>2</sub> ( $t_{2g}^6e_g^0$ ) rose by 0.157 eV/f.u. with respect to their corresponding high spin configurations. Ni ions in NaNiO<sub>2</sub>, nonetheless, are stabilized in low spin configuration as setting Ni to high spin configuration ( $t_{2g}^5e_g^2$ ) raised the total energy by 0.777 eV/f.u. Our calculations for Ni is agreement with the experimental observation of low spin NaNiO<sub>2</sub>.<sup>24</sup>

Unlike their 3d counterparts, early 4d TM ions in NaZrO<sub>2</sub> and NaNbO<sub>2</sub>, deviate from  $t_{2g}e_g$  splitting as Zr bears no magnetic moment and Nb adopts two distinct magnetic moments both significantly smaller than the anticipated  $t_{2g}^2e_g^0$ . NaZrO<sub>2</sub> in which Zr set to  $t_{2g}^1e_g^0$  was 0.317 eV/f.u. higher in energy than



Table 1 Calculated and observed lattice parameters and structural data for NaTMO<sub>2</sub> compounds in hexagonal representation

System	Calculated <i>a</i> (Å)	Calculated <i>c</i> (Å)	Experimental <i>a</i> (Å)	Experimental <i>c</i> (Å)	Ref.	TM–O (Å)	$\eta$ (°)
NaTiO <sub>2</sub>	3.042	16.551	3.037	16.260	10	2.11	92.25
NaVO <sub>2</sub>	3.055	16.242	2.996	16.100	11	2.10	95.57
NaCrO <sub>2</sub>	3.052	16.146	3.030	16.000	20	2.06	95.66
NaMnO <sub>2</sub>	3.087 <sup>a</sup>	16.234	—	—	—	2.01, 2.26	92.16 <sup>b</sup>
NaFeO <sub>2</sub>	3.061	16.286	3.029	16.113	21	2.03	94.86
NaCoO <sub>2</sub>	2.908	15.776	2.891	15.612	21	1.95	96.13
NaNiO <sub>2</sub>	3.000	15.899	2.960	15.780	6	2.02	95.89
NaZrO <sub>2</sub>	3.206	17.217	—	—	—	2.24	90.63
NaNbO <sub>2</sub>	2.998 <sup>a</sup>	17.817	—	—	—	2.22 (unpuckered), 2.18 (puckered), 2.23 (puckered)	91.15 <sup>b</sup>
NaMoO <sub>2</sub>	3.272	16.128	—	—	—	2.19	96.90
NaTcO <sub>2</sub>	3.111	16.466	—	—	—	2.14	93.12
NaRuO <sub>2</sub>	3.121	15.968	3.124	16.037	22	2.11	96.29
NaRhO <sub>2</sub>	3.151	15.725	3.097	15.527	23	2.10	97.03
NaPdO <sub>2</sub>	3.235 <sup>a</sup>	15.854	—	—	—	2.07 (Pd <sup>4+</sup> ), 2.10 (Pd <sup>3+</sup> ), 2.32 (Pd <sup>3+</sup> ), 2.27 (Pd <sup>2+</sup> )	90.00 <sup>b</sup>

<sup>a</sup> The lattice parameter *a* of the supercell has been divided by the number of hexagonal unit cells in corresponding dimensions of the supercell.

<sup>b</sup> These values correspond to the angles closest in value to 90° in distorted systems.

non-magnetic NaZrO<sub>2</sub> while NaNbO<sub>2</sub> with Nb fixed to  $t_{2g}^2 e_g^0$  configuration was 0.649 eV/f.u. higher than the presented ground state. Moreover, contrarily to the 3d TM ions, the later 4d TM ions in NaTMO<sub>2</sub> stabilized in low spin configuration. The total energy of NaTcO<sub>2</sub> rose by 1.086 eV/f.u. when Tc was set to high spin configuration ( $t_{2g}^2 e_g^2$ ). Similarly, the high spin NaRuO<sub>2</sub> ( $t_{2g}^3 e_g^2$ ) and NaRhO<sub>2</sub> ( $t_{2g}^4 e_g^2$ ) were higher in energy than their low spin counterpart by 1.937 eV/f.u. and 4.642 eV/f.u. respectively.

### 3.2. Electronic structures

Fig. 2 shows the total and partial density of states (DOS) of 3d TM containing NaTMO<sub>2</sub> compounds. In the NaTiO<sub>2</sub>,

rhombohedral distortion in the TiO<sub>6</sub> octahedra splits the  $t_{2g}$  orbitals of the spin-up channel into lower single fold  $a_{1g}$  orbital which is occupied by Ti<sup>3+</sup>'s lone 3d electron and higher empty  $e'_g$  orbitals. Furthermore,  $a_{1g}$  orbital is detached from the lower O 2p states and creates a pseudo-gap within the valence band. Consequently, the complete separation of Ti 3d states from O 2p states implies that Ti–O bond is highly ionic. In NaVO<sub>2</sub>, the rhombohedral splitting is still dominant. However, contrary to the Ti case, the occupied  $e'_g$  orbitals have lower energy than the empty  $a_{1g}$  orbital. Moreover, since the gap between  $e'_g$  states and O 2p states is now closed, there is a greater hybridization between  $e'_g$  and O 2p states which reduces the ionicity of the V–O bond compared to that of Ti–O bond. In NaCrO<sub>2</sub>, through

Table 2 Nominal electronic configuration of the d shell in NaTMO<sub>2</sub> compound, calculated number of unpaired d electrons (spin population) and the energy difference between ferromagnetic and antiferromagnetic states ( $\Delta E$ ) are given. The nominal electronic configuration corresponds to the hypothetical complete ionic bonding. The magnetic ground state and the conduction type of all compounds also summarized here. FM, AAFM, GAFM stand for ferromagnetic, A-type and G-type antiferromagnetic states respectively

Compound	Nominal configuration	Calculated unpaired d electrons	$\Delta E_{\text{CAFM}}$ (mEV)	$\Delta E_{\text{AAFM}}$ (mEV)	Magnetic ground state	Conduction
NaTiO <sub>2</sub>	$t_{2g}^1 e_g^0$	0.897	−395.365	−0.228	GAFM	Insulator
NaVO <sub>2</sub>	$t_{2g}^2 e_g^0$	1.879	−18.163	−3.204	GAFM	Insulator
NaCrO <sub>2</sub>	$t_{2g}^3 e_g^0$	2.925	−4.341	−0.323	GAFM	Insulator
NaMnO <sub>2</sub>	$t_{2g}^3 e_g^1$	3.922	51.657	0.197	FM	Insulator
NaFeO <sub>2</sub>	$t_{2g}^3 e_g^2$	4.277	−4.738	−1.894	GAFM	Insulator
NaCoO <sub>2</sub>	$t_{2g}^4 e_g^2$	3.149	152.238	−2.410	AAFM	Half metallic
NaNiO <sub>2</sub>	$t_{2g}^6 e_g^1$	1.378	24.564	0.826	FM	Half metallic
NaZrO <sub>2</sub>	$t_{2g}^1 e_g^0$	0.000	—	—	Nonmagnetic	Metallic
NaNbO <sub>2</sub>	$t_{2g}^2 e_g^0$	1.110, 0.350	14.468	−1.240	AAFM	Metallic
NaMoO <sub>2</sub>	$t_{2g}^3 e_g^0$	2.567	−117.673	−2.272	GAFM	Insulator
NaTcO <sub>2</sub>	$t_{2g}^4 e_g^0$	1.721	65.860	2.565	FM	Half metallic
NaRuO <sub>2</sub>	$t_{2g}^5 e_g^0$	0.858	−13.462	−5.030	GAFM	Insulator
NaRhO <sub>2</sub>	$t_{2g}^6 e_g^0$	0.000	—	—	Nonmagnetic	Insulator
NaPdO <sub>2</sub>	$t_{2g}^6 e_g^2$	1.339	11.315	−2.750	AAFM	Insulator
	$t_{2g}^6 e_g^1$	0.621				
	$t_{2g}^6 e_g^0$	0.015				





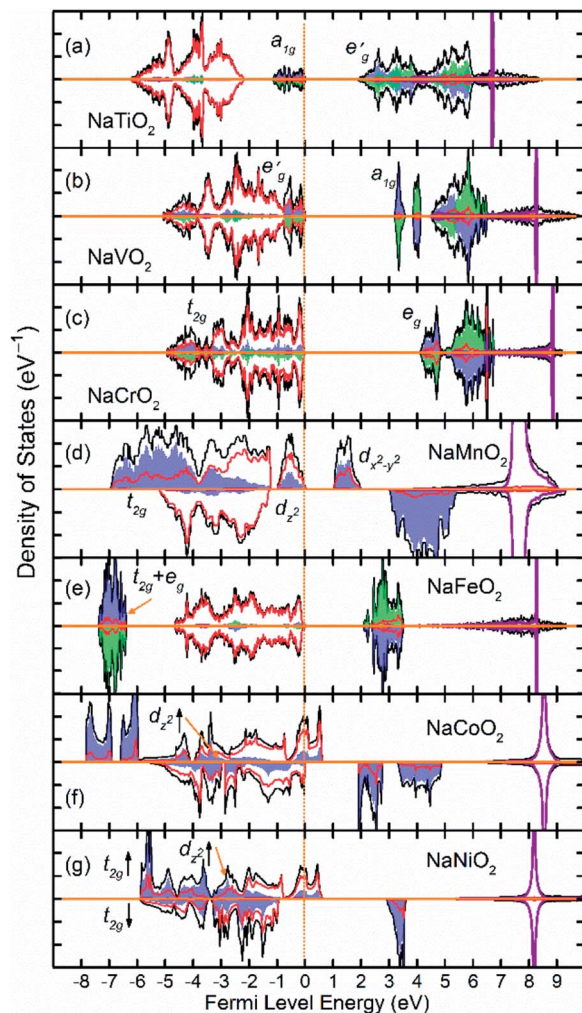


Fig. 2 The density of states (DOS) of NaTMO<sub>2</sub> compounds in which TM is fourth row transition metal element. The black, red and purple lines correspond to total, O 2p and Na states respectively. The blue and green shaded areas correspond to TM 3d elements with net spin-up and spin-down electronic population respectively. Compounds with only blue shaded areas are either non-magnetic or those with inter-plane ferromagnetic coupling.

the merging of the  $e'_g$  and  $a_{1g}$  states in the spin-up channel, the band structure resembles conventional octahedral splitting where the spin-up  $t_{2g}$  states in the valence band are all occupied while the empty  $e_g$  states constitute the bottom of the conduction band. The DOS of NaMnO<sub>2</sub> corresponds to the elongated Jahn–Teller distortion. The lower region of the valence band ( $\sim -7 \text{ eV} < E < \sim -4 \text{ eV}$ ) is occupied by  $d_{xz}$  and  $d_{yz}$  states while the middle part ( $\sim -4 \text{ eV} < E < \sim -1.2$ ) is occupied by  $d_{xy}$  states. The top of valence band is nevertheless occupied by  $d_{z^2}$  states. As inferred from the DOS, the proximity of  $d_{xy}$  and  $d_{z^2}$  favors the high spin configuration for the Mn ions.

The DOS of the half-filled Fe 3d shell ( $t_{2g}^3 e_g^2$ ) in NaFeO<sub>2</sub> exhibits a different arrangement when compared to earlier compounds. Here, due to strong electron–electron repulsion between the half-filled Fe 3d<sup>5</sup> states and O 2p states, all of the occupied Fe 3d states are shifted downwards below O 2p states.

The proximity of the  $t_{2g}^3$  and  $e_g^2$  states in the spin-up channel to one another favors the high spin configuration for Fe ions as the spin-down  $t_{2g}$  states are  $\sim 11 \text{ eV}$  higher in energy than spin-up  $e_g$  states. In NaCoO<sub>2</sub>, the  $t_{2g}$  states of the spin-up channel, although mainly concentrate at the bottom of the valence band, still stretch over the entire valence band width and strongly hybridize with O 2p states. Furthermore, the tail of the spin-up  $t_{2g}$  states crosses the Fermi level creating half metallic conduction. Similarly, in NaNiO<sub>2</sub>, the spin-up  $t_{2g}$  states stretch over the valence band and cross the Fermi level while the spin-down  $t_{2g}$  states and  $d_{z^2}$  states remain confined within the middle of the valence band without crossing the Fermi level.

Fig. 3 shows the total and partial DOS in 4d TM containing compounds. NaZrO<sub>2</sub> exhibits strong metallic character as its Fermi level intercepts the Zr 4d states in the conduction band. Metallicity in NaZrO<sub>2</sub> is facilitated by a metallic Zr–Zr bond which is caused by extraordinarily large Zr<sup>3+</sup> ionic radius of

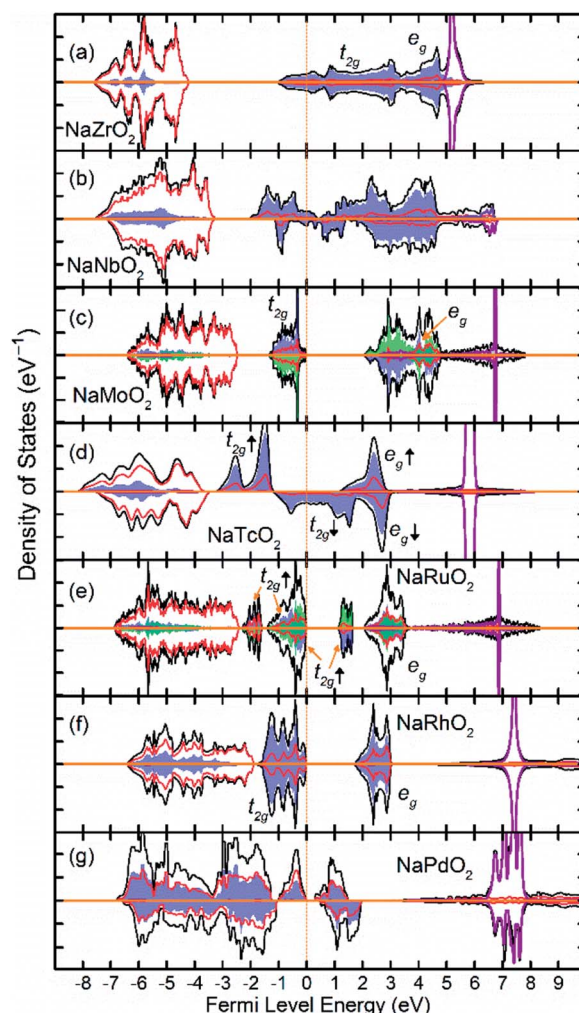


Fig. 3 The density of states (DOS) of NaTMO<sub>2</sub> compounds in which TM is fifth row transition metal element. The black, red and purple lines correspond to total, O 2p and Na states respectively. The blue and green shaded areas correspond to TM 4d elements with net spin-up and spin-down electronic population respectively. Compounds with both blue and green shaded areas are G-type antiferromagnetic.



$\sim 0.89$  Å (ref. 25) and the Zr–Zr distance of 3.21 Å which is comparable to that in Zr metal. The metallic character of NaZrO<sub>2</sub> explains the lack of magnetic moment as there is no significant hybridization between Zr with O. NaNbO<sub>2</sub> also exhibits metallic conduction as the Fermi level crosses through the 4d states in the conduction band. However, as we will discuss later, due to puckering distortion, there are two distinct Nb species in this compound each with different levels of metallicity. The band structure of the NaMoO<sub>2</sub> shows a conventional octahedral distortion where the half-filled  $t_{2g}$  states constitute the top of the valence band while the empty  $e_g$  states are separated by  $\sim 1$  eV above the Fermi level. In NaTcO<sub>2</sub>, NaRuO<sub>2</sub> and NaRhO<sub>2</sub> compounds the spin-down channel of the  $t_{2g}$  states is progressively filled as expected for the TM ions in low spin configuration. As will be discussed in detail in the next section, Pd in NaPdO<sub>2</sub> undergoes charge disproportionation and form Pd<sup>2+</sup>, Pd<sup>3+</sup>, Pd<sup>4+</sup> species. The  $t_{2g}$  states of all Pd species occupy the lower part of the conduction band while the filled  $e_g$  occupy the top of the valence band.

### 3.3. Octahedral distortions

The geometry optimization conducted with larger supercells revealed that NaMnO<sub>2</sub>, NaNbO<sub>2</sub> and NaPdO<sub>2</sub> compounds, each to a different extent, exhibits additional distortions in their TMO<sub>6</sub> octahedra. In NaMnO<sub>2</sub>, as indicated by purple arrows in Fig. 4, two out of six Mn–O bonds in all MnO<sub>6</sub> octahedra are elongated causing a deviation from perfect  $R\bar{3}m$  symmetry. This distortion is similar to the Jahn–Teller distortion depicted in Fig. 1(e). The long Mn–O bond is 2.26 Å while the short Mn–O bonds is 2.01 Å implying a 12.4% elongation. We found that perfectly  $R\bar{3}m$  symmetric NaMnO<sub>2</sub> primitive cell with no elongation had a total energy 0.763 eV/f.u. higher than the distorted compound indicating that this distortion leads to significant stabilization.

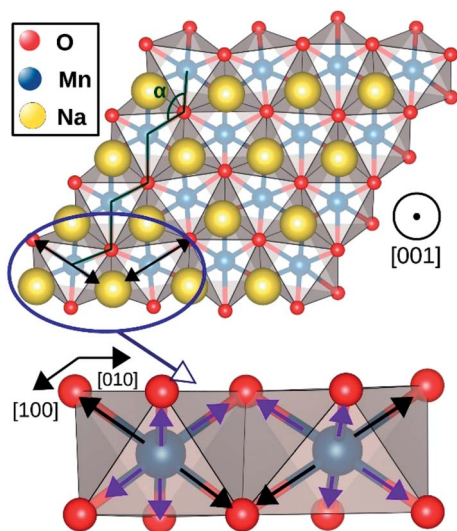


Fig. 4 Jahn–Teller distortion in NaMnO<sub>2</sub> system. The elongated bonds are marked with black arrows while the shorter bonds are marked with purple arrows.

NaNbO<sub>2</sub> showed puckering distortion [Fig. 1(f)] in half of its NbO<sub>6</sub> octahedra. As marked by blue arrows in Fig. 5(a), NbO<sub>6</sub> octahedra on every second row in [100] direction are alternately puckered to the left and the right along [010] direction while the octahedra on the adjacent row only had rhombohedral distortion. In the puckered NbO<sub>6</sub> octahedra, the short Nb–O bond was 2.18 Å while the long Nb–O bond was 2.23 Å indicating a 2.2% puckering distortion in bond lengths. The bond length in unpuckered NbO<sub>6</sub> octahedra had a median value of 2.22 Å. The puckering altered the electronic structure of the NaNbO<sub>2</sub> compound as ions in the puckered and unpuckered octahedra had distinct spin populations of 1.051e and 0.350e respectively. According to Fig. 5(b), Nb ions in the puckered octahedra has a significantly larger spin-up population (marked with red arrow) and smaller spin-down population (marked with blue arrow) compared to the Nb ions in unpuckered octahedra. To examine the stability induced by this distortion, we once set all Nb ions to low magnetization equal to that in the unpuckered octahedra and once again to high magnetization equal to that in the puckered octahedra and recalculated the total energy. The earlier setting raised the total energy of NaNbO<sub>2</sub> compound by 0.230 eV/f.u. while the latter setting raised the total energy by 0.649 eV/f.u. demonstrating the stabilizing effect of puckering distortion. Given that Nb's total electronic population does not significantly depend on the puckering of NbO<sub>6</sub> octahedra, we infer that this relatively minor distortion does not cause charge disproportionation but rather only alters the magnetization of Nb ions.

The distortion in PdO<sub>6</sub> octahedra in NbPdO<sub>2</sub> were accompanied with charge disproportionation among Pd ions. As

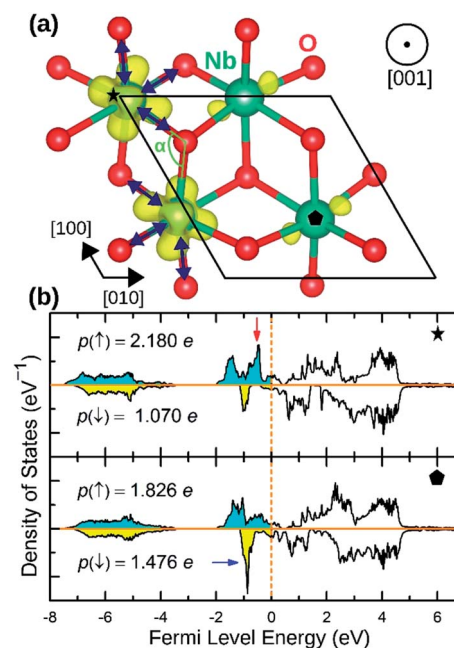


Fig. 5 (a) The spin density isosurface of NaNbO<sub>2</sub> drawn at 0.025 e Å<sup>-2</sup>. Half of the NbO<sub>6</sub> octahedra undergo puckering distortion. The compressed bonds are marked with blue arrows. (b) The site-projected Nb 4d states for high magnetization (top panel) and low magnetization (bottom panel) Nb species.





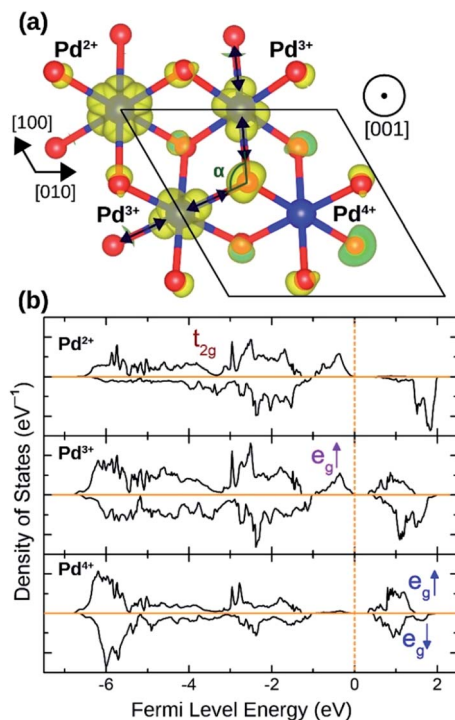


Fig. 6 (a) The spin density isosurface in NaPdO<sub>2</sub> drawn at 0.025 e Å<sup>-2</sup> demonstrating charge disproportionation. (b) The site-projected 4d states for Pd<sup>2+</sup>, Pd<sup>3+</sup> and Pd<sup>4+</sup> species.

shown in Fig. 6(a), within a Pd containing plane perpendicular to the [001] direction in the  $2a \times 2a \times 1c$  supercell, two Pd<sup>3+</sup> ions transform into a pair of Pd<sup>4+</sup> and Pd<sup>2+</sup> along [110] direction while the other two Pd<sup>3+</sup> ions along [1 $\bar{1}$ 0] direction remain unchanged. The Pd<sup>2+</sup>O<sub>6</sub> and Pd<sup>4+</sup>O<sub>6</sub> octahedra had perfect octahedral symmetry however each with a different Pd–O bond length. Pd<sup>2+</sup>–O bond was 2.27 Å long while Pd<sup>4+</sup>–O bond was 2.07 Å long. The two Pd<sup>3+</sup>O<sub>6</sub> octahedra, on the other hand, showed elongated Jahn–Teller distortion with long bonds of 2.32 Å and short bonds of 2.09 Å accounting for an elongation of 11.0%. The stability of this distortion was verified by the fact that the NaPdO<sub>2</sub> in which all Pd ions were fixed to +3 oxidation state had a total energy 0.381 eV/f.u. higher than the presented ground state. Furthermore, this distortion pattern and the accompanying charge disproportionation prevailed in larger  $4a \times 4a \times 1c$  supercell and persisted under different  $U_{\text{eff}}$  values.

Fig. 6(b) shows how Pd  $e_g$  states are occupied as charge disproportionation occurs. For Pd<sup>2+</sup>,  $e_g$ 's spin-up states are all occupied while the empty spin-down states are entirely located  $\sim 1$  eV above the Fermi level. For Pd<sup>3+</sup>, the spin-up peak decreases (marked with a red arrow) while an empty spin-up  $e_g$  peak appears above the Fermi level. Finally, for Pd<sup>4+</sup>, all  $e_g$  states are now located above the Fermi level.

### 3.4. Magnetic coupling

The magnetic ground state of a compound can be predicted by comparing the total energies corresponding to different spin alignments among the TM ions that is  $\Delta E_{\text{CAFM}}$  and  $\Delta E_{\text{AAFM}}$ .<sup>26</sup> If

different spin alignments result in the same energy, the compound is paramagnetic.<sup>27</sup> Furthermore,  $\Delta E_{\text{CAFM}}$  and  $\Delta E_{\text{AAFM}}$  are functions of the magnetic exchange integrals ( $J$ ) which determine the Curie and Néel temperatures ( $T_C$  and  $T_N$ ) in compounds with long range magnetic ordering.<sup>28</sup> According to the mean field approximation these critical temperatures depends linearly on the  $J$ .<sup>29</sup> For instance, room temperature ferromagnetism requires positive  $\Delta E_{\text{CAFM}}$  and  $\Delta E_{\text{AAFM}}$  values of  $\sim 12$  meV.<sup>30</sup>

As presented in Table 2, NaMnO<sub>2</sub>, NaCoO<sub>2</sub>, NaNiO<sub>2</sub>, NaNbO<sub>2</sub>, NaTcO<sub>2</sub> and NaPdO<sub>2</sub> have positive  $\Delta E_{\text{CAFM}}$  values indicating inter-plane ferromagnetism which is defined as the ferromagnetic coupling among TM ions within the basal TMO<sub>2</sub> planes. This ferromagnetic coupling can be attributed to one of two distinct mechanisms: the kinetic p–d exchange interaction and the superexchange interaction. The density of states in Fig. 2(f)–(g) and Fig. 3(d) reveals a special p–d hybridization in NaCoO<sub>2</sub>, NaNiO<sub>2</sub> and NaTcO<sub>2</sub> compounds. Because of this hybridization, the spin majority p states are shifted to higher energies, while the spin minority p states are shifted to lower energies. This hybridization scheme therefore creates spin polarized p states which mediate the ferromagnetic coupling.<sup>29</sup> In NaMnO<sub>2</sub>, NaNbO<sub>2</sub> and NaPdO<sub>2</sub>, on the other hand, positive  $\Delta E_{\text{CAFM}}$  values are caused by ferromagnetic superexchange. The prerequisite for ferromagnetic superexchange is a  $\sim 90^\circ$  TM–O–TM angle which stabilizes the ferromagnetic coupling through  $\pi$  TM–O bonds in TM–O–TM trimer.<sup>31</sup> The octahedral distortions in these compounds orient the TM–O–TM angles in these compounds to  $\sim 90^\circ$ . Under perfect  $R\bar{3}m$  symmetry, as shown in Fig. 1(c), the TM–O–TM angle is determined by O's fractional coordinates and alternates between the supplementary angles  $\eta$  and  $\theta$  [defined in Fig. 1(c) and (d)] preventing the stabilization of the ferromagnetic phase.<sup>9,11,32,33</sup> If a distortion, however, breaks the symmetry and brings the TM–O–TM angle closer to  $90^\circ$ , ferromagnetic superexchange can prevail. One should note that, as indicated in Table 1, the octahedral distortions in these compounds basically bring the O–TM–O angle closer to  $90^\circ$ . However, since these compounds do not have any octahedral tilting, the TM–O–TM angle, at least in certain planes, also approaches  $90^\circ$  due to the similar distortion in neighbouring TMO<sub>6</sub> octahedra. Those TM–O–TM angles assisting the ferromagnetic superexchange are marked  $\alpha$  in Fig. 4–6.  $\alpha$  is  $91.67^\circ$  in NaMnO<sub>2</sub>,  $89.86^\circ$  in NaNbO<sub>2</sub> and  $88.48^\circ$  in NaPdO<sub>2</sub>. Contrary to our results, earlier DFT calculation of the NaMnO<sub>2</sub> compound using a small supercell restricted to  $C2/m$  symmetry, predicted weak frustrated antiferromagnetic ground state.<sup>34</sup> This discrepancy shows the importance of taking into account the octahedral distortions that stabilizes the ferromagnetic ground state. Inferred from  $\Delta E_{\text{CAFM}}$  values, the kinetic p–d exchange interaction seems to be generally stronger than the ferromagnetic superexchange interaction.

The magnetic coupling across the TMO<sub>2</sub> planes or intra-plane coupling, in principle, can be mediated a by second nearest neighbour superexchange interaction through TM–O–Na–O–TM chain *via* by O's p orbitals and Na  $sp^2$  hybrid orbitals.<sup>35</sup> Because of anisotropy in the  $R\bar{3}m$  crystal structure which prevents the hybridization of TM d states with the p



states of adjacent TMO<sub>2</sub> layers, p–d kinetic exchange is not expected to result in significant intra-plane coupling. Among all compounds only NaMnO<sub>2</sub>, NaNiO<sub>2</sub> and NaTcO<sub>2</sub> had small positive  $\Delta E_{\text{AAFM}}$  values indicating weak ferromagnetic intra-plane coupling resulting in  $T_{\text{C}}$  values lower than  $\sim 50$  K. This prediction, particularly for the NaNiO<sub>2</sub> compound, is agreement with the earlier observation that measured a  $T_{\text{C}}$  of  $\sim 20$  K.<sup>7</sup> In the case of NaNbO<sub>2</sub>, NaPdO<sub>2</sub> and NaCoO<sub>2</sub> compounds, the negative  $\Delta E_{\text{AAFM}}$  values along with positive  $\Delta E_{\text{CAFM}}$  values predict A-type antiferromagnetic ground state. For the rest of compounds for which both  $\Delta E_{\text{AAFM}}$  and  $\Delta E_{\text{CAFM}}$  are negative, G-type antiferromagnetic ground state prevails. Such antiferromagnetism has been observed in NaCrO<sub>2</sub> with  $T_{\text{N}} = 40\text{--}50$  K,<sup>36,37</sup> NaVO<sub>2</sub> (ref. 11 and 38) and NaTiO<sub>2</sub> (ref. 39).

Last, note that relativistic spin–orbit interaction can play a significant role in determining the structural and magnetic properties of isolated TM octahedral complexes.<sup>40–43</sup> However, in the context of bulk NaTMO<sub>2</sub> compounds that have been studied here, the role of spin–orbit interaction on the calculated  $\Delta E_{\text{CAFM}}$  and  $\Delta E_{\text{AAFM}}$  values is negligibly small. Spin–orbit interaction constant is proportional to the mass of the interacting ions and can be significant in 5d TM oxides such as iridates.<sup>44</sup> However, experimental studies have shown that the magnitude of the spin–orbit interaction in 3d and 4d TM oxides such as cobaltates<sup>45</sup> and rhoates<sup>46</sup> is generally small. To verify this notion, we recalculated the  $\Delta E_{\text{CAFM}}$  and  $\Delta E_{\text{AAFM}}$  for NaPdO<sub>2</sub> with the inclusion of the spin–orbit calculation and obtained  $\Delta E_{\text{CAFM}} = 11.492$  meV and  $\Delta E_{\text{AAFM}} = -2.841$  meV. These values differ only by  $\sim 0.1$  meV from the values of Table 2 which have been obtained without including spin–orbit interaction. The role of spin–orbit interaction is expected to be even smaller for the rest of the compounds, especially for 3d NaTMO<sub>2</sub>, as their molecular mass is considerably smaller than that of NaPdO<sub>2</sub>.

## 4. Conclusions

We demonstrated that the rhombohedral distortion inherent to the  $3\bar{R}m$  symmetry stabilizes G-type antiferromagnetism in NaTiO<sub>2</sub>, NaVO<sub>2</sub>, NaCrO<sub>2</sub>, NaFeO<sub>2</sub>, NaMoO<sub>2</sub> and NaRuO<sub>2</sub> compounds. Inter-plane ferromagnetism however can be stabilized if the  $3\bar{R}m$  symmetry breaks due to additional octahedral distortions which is the case for NaMnO<sub>2</sub>, NaNbO<sub>2</sub> and NbPdO<sub>2</sub>. Here, because of favorable orbital orientation, the superexchange interaction stabilizes ferromagnetism instead of antiferromagnetism among the TM ions of the same TMO<sub>2</sub> plane. Additionally, strong p–d hybridization, as in NaCoO<sub>2</sub>, NaNiO<sub>2</sub> and NaTcO<sub>2</sub> can also result in inter-plane ferromagnetism. In this case, due to its strength, the kinetic p–d exchange mechanism overcomes the underlying inter-plane antiferromagnetism. The intra-plane ferromagnetic coupling is mediated by a weak second neighbor coupling which prevails only in NaMnO<sub>2</sub>, NaTcO<sub>2</sub> and NaNiO<sub>2</sub> giving rise to bulk ferromagnetism with low  $T_{\text{C}}$ .

The weak intra-plane coupling appears to be a general feature of O3 compounds. This is in contrast to the P2 structures in which the magnitudes of inter-plane and intra-plane coupling are of the same order.<sup>35</sup> This is probably because

this interaction strongly depends on Na's coordination environment. This line of enquiry warrants further research.

## Conflicts of interest

The authors declare no competing financial interest.

## Acknowledgements

This work was supported in part by MEXT as a social and scientific priority issue: creation of new functional devices and high-performance materials to support next-generation industries to be tackled by using post-K computer. Computational resources were provided by Kyushu University's high performance computing center and supercomputers at the Institute for Solid State Physics at the University of Tokyo and at the Center for Computational Sciences at University of Tsukuba.

## References

- 1 M. V. Mostovoy and D. I. Khomskii, *Phys. Rev. Lett.*, 2002, **89**, 227203.
- 2 O. I. Velikokhatnyi, C.-C. Chang and P. N. Kumta, *J. Electrochem. Soc.*, 2003, **150**, A1262–A1266.
- 3 L. Viciu, J. W. G. Bos, H. W. Zandbergen, Q. Huang, M. L. Foo, S. Ishiwata, A. P. Ramirez, M. Lee, N. P. Ong and R. J. Cava, *Phys. Rev. B: Condens. Matter Mater. Phys.*, 2006, **73**, 174104.
- 4 S. Walia, S. Balendhran, H. Nili, S. Zhuiykov, G. Rosengarten, Q. H. Wang, M. Bhaskaran, S. Sriram, M. S. Strano and K. Kalantar-zadeh, *Prog. Mater. Sci.*, 2013, **58**, 1443–1489.
- 5 M. D. Slater, D. Kim, E. Lee and C. S. Johnson, *Adv. Funct. Mater.*, 2013, **23**, 947–958.
- 6 E. Chappel, M. D. Nunez-Regueiro, F. Dupont, G. Chouteau, C. Darie and A. Sulpice, *Eur. Phys. J. B*, 2000, **17**, 609–614.
- 7 S. d. Brion, M. Bonda, C. Darie, P. Bordet and I. Sheikin, *J. Phys.: Condens. Matter*, 2010, **22**, 126001.
- 8 T. A. Kaplan and N. Menyuk, *Philos. Mag.*, 2007, **87**, 3711–3785.
- 9 N. Terada, Y. Ikeda, H. Sato, D. D. Khalyavin, P. Manuel, A. Miyake, A. Matsuo, M. Tokunaga and K. Kindo, *Phys. Rev. B: Condens. Matter Mater. Phys.*, 2017, **96**, 035128.
- 10 D. Wu, X. Li, B. Xu, N. Twu, L. Liu and G. Ceder, *Energy Environ. Sci.*, 2015, **8**, 195–202.
- 11 T. Jia, G. Zhang, Z. Zeng and H. Q. Lin, *Phys. Rev. B: Condens. Matter Mater. Phys.*, 2009, **80**, 045103.
- 12 G. Kresse and D. Joubert, *Phys. Rev. B: Condens. Matter Mater. Phys.*, 1999, **59**, 1758–1775.
- 13 G. Kresse and J. Furthmüller, *Phys. Rev. B: Condens. Matter Mater. Phys.*, 1996, **54**, 11169–11186.
- 14 G. Kresse and J. Furthmüller, *Comput. Mater. Sci.*, 1996, **6**, 15–50.
- 15 S. Maintz, V. L. Deringer, A. L. Tchougréeff and R. Dronskowski, *J. Comput. Chem.*, 2016, **37**, 1030–1035.
- 16 J. P. Perdew, K. Burke and M. Ernzerhof, *Phys. Rev. Lett.*, 1996, **77**, 3865–3868.





- 17 J. P. Perdew, K. Burke and M. Ernzerhof, *Phys. Rev. Lett.*, 1997, **78**, 1396.
- 18 S. Dudarev, G. Botton, S. Savrasov, C. Humphreys and A. Sutton, *Phys. Rev. B: Condens. Matter Mater. Phys.*, 1998, **57**, 1505–1509.
- 19 P. Gopal and N. A. Spaldin, *Phys. Rev. B: Condens. Matter Mater. Phys.*, 2006, **74**, 094418.
- 20 Y.-N. Zhou, J.-J. Ding, K.-W. Nam, X. Yu, S.-M. Bak, E. Hu, J. Liu, J. Bai, H. Li, Z.-W. Fu and X.-Q. Yang, *J. Mater. Chem. A*, 2013, **1**, 11130–11134.
- 21 K. Kubota, T. Asari, H. Yoshida, N. Yaabuuchi, H. Shiiba, M. Nakayama and S. Komaba, *Adv. Funct. Mater.*, 2016, **26**, 6047–6059.
- 22 K. M. Mogare, K. Friese, W. Klein and M. Jansen, *Z. Anorg. Allg. Chem.*, 2004, **630**, 547–552.
- 23 K. Hobbie and R. Hoppe, *Z. Anorg. Allg. Chem.*, 1988, **565**, 106–110.
- 24 E. Chappel, M. D. Núñez-Regueiro, G. Chouteau, O. Isnard and C. Darie, *Eur. Phys. J. B*, 2000, **17**, 615–622.
- 25 S. Jeon, J. Ryu, H.-G. Shin, J. Lee and H. Lee, *Mater. Charact.*, 2017, **131**, 374–379.
- 26 K. Sato, L. Bergqvist, J. Kudrnovský, P. H. Dederichs, O. Eriksson, I. Turek, B. Sanyal, G. Bouzerar, H. Katayama-Yoshida, V. A. Dinh, T. Fukushima, H. Kizaki and R. Zeller, *Rev. Mod. Phys.*, 2010, **82**, 1633–1690.
- 27 M. H. N. Assadi and H. Katayama-Yoshida, *Funct. Mater. Lett.*, 2015, **08**, 1540016.
- 28 J. Lee, PhD thesis, The University of Texas at Austin, 2010.
- 29 B. Belhadji, L. Bergqvist, R. Zeller, P. H. Dederichs, K. Sato and H. Katayama-Yoshida, *J. Phys.: Condens. Matter*, 2007, **19**, 436227.
- 30 P. W. Anderson, in *Solid State Physics*, ed. F. Seitz and D. Turnbull, Academic Press, 1963, vol. 14, pp. 99–214.
- 31 J. M. D. Coey, M. Venkatesan and H. Xu, in *Functional Metal Oxides*, Wiley-VCH Verlag GmbH & Co. KGaA, 2013, pp. 1–49, DOI: 10.1002/9783527654864.ch1.
- 32 K. Takada, H. Sakurai, E. Takayama-Muromachi, F. Izumi, R. A. Dilanian and T. Sasaki, *Nature*, 2003, **422**, 53–55.
- 33 S. P. Bayrakci, I. Mirebeau, P. Bourges, Y. Sidis, M. Enderle, J. Mesot, D. P. Chen, C. T. Lin and B. Keimer, *Phys. Rev. Lett.*, 2005, **94**, 157205.
- 34 G. R. Zhang, L. J. Zou, Z. Zeng and H. Q. Lin, *J. Appl. Phys.*, 2009, **105**, 07E512.
- 35 M. D. Johannes, I. I. Mazin and D. J. Singh, *Phys. Rev. B: Condens. Matter Mater. Phys.*, 2005, **71**, 214410.
- 36 D. Hsieh, D. Qian, R. F. Berger, R. J. Cava, J. W. Lynn, Q. Huang and M. Z. Hasan, *Phys. B*, 2008, **403**, 1341–1343.
- 37 A. Olariu, P. Mendels, F. Bert, B. G. Ueland, P. Schiffer, R. F. Berger and R. J. Cava, *Phys. Rev. Lett.*, 2006, **97**, 167203.
- 38 T. M. McQueen, P. W. Stephens, Q. Huang, T. Klimczuk, F. Ronning and R. J. Cava, *Phys. Rev. Lett.*, 2008, **101**, 166402.
- 39 I. Yamada, K. Ubukoshi and K. Hirakawa, *J. Phys. Soc. Jpn.*, 1985, **54**, 3571–3576.
- 40 J. David and A. Restrepo, *Phys. Rev. A*, 2007, **76**, 052511.
- 41 J. David, P. Fuentealba and A. Restrepo, *Chem. Phys. Lett.*, 2008, **457**, 42–44.
- 42 A. Pérez-Villa, J. David, P. Fuentealba and A. Restrepo, *Chem. Phys. Lett.*, 2011, **507**, 57–62.
- 43 J. David, D. Guerra and A. Restrepo, *Inorg. Chem.*, 2011, **50**, 1480–1483.
- 44 Y. Singh, S. Manni, J. Reuther, T. Berlijn, R. Thomale, W. Ku, S. Trebst and P. Gegenwart, *Phys. Rev. Lett.*, 2012, **108**, 127203.
- 45 Y. Yanase, M. Mochizuki and M. Ogata, *J. Phys. Soc. Jpn.*, 2005, **74**, 2568–2578.
- 46 I. I. Mazin, S. Manni, K. Foyevtsova, H. O. Jeschke, P. Gegenwart and R. Valentí, *Phys. Rev. B: Condens. Matter Mater. Phys.*, 2013, **88**, 035115.

